Sound and vorticity interactions: transmission and scattering

Jean-François Pinton, Guillaume Brillant

Theoret. Comput. Fluid Dynamics (2004)
Digital Object Identifier (DOI) 10.1007/s00162-004-0150-4

Theoretical and Computational Fluid Dynamics

Original article

Sound and vorticity interactions: transmission and scattering

Jean-François Pinton, Guillaume Brillant

École Normale Supérieure de Lyon, Laboratoire de Physique, 46 allée d'Italie, 69007 Lyon, France

Received September 2, 2003 / Accepted July 14, 2004
Published online October 29, 2004 – © Springer-Verlag 2004
Communicated by T. Colonius

Abstract. We review several aspects of the propagation of sound in vortical flows. We restrict ourselves to isothermal, humidity-free flows at low Mach number M. Since vorticity plays a major role in vortex-flow interactions we focus on vortical flows. We consider two main canonical situations. The first concerns the transmission of sound. We analyze the evolution of acoustic wavefronts as they propagate across a single vortex. The second situation addresses the scattering of sound waves by nonstationary vortices. We study the evolution of the acoustic pressure emitted in the far field, at an angle with the initial direction of propagation. In this geometry one performs direct spectroscopy of the flow vorticity field. In each case, we review theoretical results and compare with experimental measurements and numerical simulations when available. We also briefly report how the following new acoustic techniques have recently been used to study complex or turbulent flows: time-resolved acoustic spectroscopy, speckle interferometry and Lagrangian particle tracking.

Key words: sound, vorticity, scattering, flow, turbulence
PACS: 43.25, 43.28, 47.32, 67.40

1 Introduction

We consider the propagation of acoustic waves of weak amplitude in low Mach number flows. In this case, the flow is unmodified by the presence of the sound waves, but the sound propagation is modified by the flow. It is a situation of theoretical interest for the understanding of wave and matter interactions, and of practical importance because waves can be used as probes for the study of media that interact with them.

Sound waves are longitudinal vibrations; their propagation in a fluid flow is influenced by the presence of velocity gradients [1, 2]. When the flow is isothermal (i.e., when the effect of temperature fluctuations can be neglected), the leading contribution to transmission and scattering effects comes from the antisymmetric part of the velocity gradients, i.e., from the vorticity of the flow. First, vortices tend to bend the direction of propagation of acoustic rays [3–5]. In addition, unsteady vortices act as sources of sound and this provides a general scattering mechanism. When a sound wave impacts a vortex, it advects it harmonically and additional sound is generated at the frequency of the incoming wave [6, 8, 9]. There is thus a strong motivation to study the interaction of a sound wave with vortex structures.

Correspondence to: J.-F. Pinton (e-mail: pinton@ens-lyon.fr)

We review here experimental investigations of the effect of isolated vortices on the propagation and scattering of incident (plane) monochromatic sound waves. We begin in Sect. II with the case of a single isolated vortex. We report measurements of the evolution of the wavefronts as a function of the distance downstream of the vortex, and also at varying ratios of sound wavelength λ to vortex core size a. In this way, one accesses the transition from a simple geometrical acoustic regime (when $ka \gg a$, $k = 2\pi/\lambda$ is the wavenumber) to a scattering regime ($ka \sim 1$). We then consider in Sect. III the scattering of sound by vortices in the single scattering regime using two examples. In the first one the vorticity distribution is that of a vortex array (the von Kármán vortex street) and in the second example we probe the vorticity filaments that form intermittently in fully developed turbulence. This article ends with a presentation in Sect. IV of new acoustic techniques used in the study of complex flows: time-resolved vorticity spectroscopy, speckle interferometry and Lagrangian particle tracking.

2 Transmission

A Theoretical background

We briefly recall the equations governing the propagation of sound in moving media. Our approach and formalism are inspired from the works of Blockintzev [3], Lighthill [6], and Howe [7]. We consider the case of a sound wave with frequency ν_0 propagating through a vortex with characteristic vorticity $\vec{\omega}$ – the geometry is schematically drawn in Fig. 1. We assume that the vortex rotation rate is much slower than the period of sound waves ($\nu_0 \gg \omega$) and that the Mach number of the flow is small ($M \sim 0.01$ in water, to $M \sim 0.1$ in gases). We further assume that the fluid flow is not disturbed by the incoming sound. Rather we concentrate on how the sound field is modified by the vortex flow. This approximation is justified by the fact that typical incident sound pressures are of the order of 1 Pa, whereas the flow pressure head $\left(\rho_0 u_0^2\right)$ is of the order of 100 Pa for most air-flows.

1 Wave equation

The momentum equation for the fluid motion reads:

$$\begin{aligned}(\rho_0+\rho')\left\{(\partial_t\vec{u}_0+\partial_t\vec{u}')+(\vec{u}_0+\vec{u}')\vec{\nabla}(\vec{u}_0+\vec{u}')\right\}\\ =\vec{\nabla}(p_0+p')\,,\end{aligned} \tag{1}$$

where the null subscript refers to the undisturbed flow and the prime quantities represent the acoustic field, treated as a perturbation. To first order, one has:

$$\rho_0\left(\partial_t\vec{u}_0+\vec{u}_0\vec{\nabla}\vec{u}_0\right)=\vec{\nabla}p_0\,, \tag{2}$$

which is the equation of motion of the undisturbed flow. At this stage, viscosity terms could be added since we only neglect viscous

attenuation for the sound wave (attenuation of sound by molecular viscosity η only occurs at very high frequencies of the order of $\rho_0 c^2/\eta$). Subtracting (2) from (1), and linearizing yields the equation for the sound wave:

$$\underbrace{\rho'\partial_t\vec{u}_0}_{A}+\underbrace{\rho_0\partial_t\vec{u}'}_{B}+\rho_0\vec{u}_0\vec{\nabla}\vec{u}'+\underbrace{\rho_0\vec{u}'\vec{\nabla}\vec{u}_0}_{C}+\underbrace{\rho'\vec{u}_0\vec{\nabla}\vec{u}_0}_{D}=\vec{\nabla}p'\,. \tag{3}$$

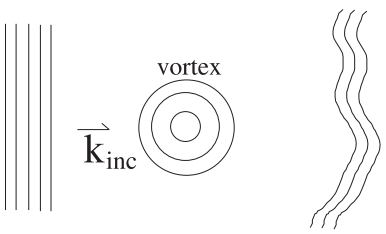

Fig. 1. Schematics of a transmission experiment. An initial plane wave at frequency ν_0 propagating in direction $\vec{k}_{inc}$, impacts an isolated vortex. The wavefronts are analyzed after they have propagated through the vortex

The order of magnitude of the various terms in the above equation can be estimated:

$$\frac{A}{B} \sim \frac{\rho' \omega u_0}{\rho_0 \nu_0 u'} \sim \frac{\omega}{\nu_0} \frac{u_0 p'/c^2}{\rho_0 u'} \sim \frac{\omega}{\nu_0} \frac{\rho_0 c u' u_0/c^2}{\rho_0 u'} = \frac{\omega}{\nu_0} M$$

$$\frac{D}{C} \sim \frac{\rho' u_0}{\rho_0 u'} \sim \frac{u_0}{u'} \frac{p'/c^2}{\rho_0} \sim \frac{u_0}{u'} \frac{\rho_0 c u'}{\rho_0 c^2} = M$$

so that at low Mach number the momentum equation reduces to:

$$\rho_0 \left(\partial_t + \vec{u}_0 \vec{\nabla}\right) \vec{u}' + \rho_0 \vec{u}' \vec{\nabla} \vec{u}_0 = \vec{\nabla} p' \,. \tag{4}$$

This equation must be supplemented by the equation of continuity:

$$\partial_t \left(\rho' + \rho_0\right) + \vec{\nabla}. \left(\rho_0 \vec{u}_0 + \rho' \vec{u}_0 + \rho_0 \vec{u}' + \rho' \vec{u}'\right) = 0 \,. \tag{5}$$

To first order, this is the mass conservation equation for the hydrodynamic flow, which we assume to be incompressible. At second order, it yields:

$$\left(\partial_t + \vec{u}_0 \vec{\nabla}\right) \rho' = -\rho_0 \vec{\nabla}.\vec{u}' \,, \tag{6}$$

which is the mass equation for the acoustic flow.

The equation that governs the propagation of the sound wave across the flow is obtained by taking the divergence of (4) and using (6). After some algebra, one has:

$$\left(\partial_t + \vec{u}_0 \vec{\nabla}\right)^2 \rho' - c^2 \Delta \rho' = -2\rho_0 \left(\partial_j u_{0,i}\right) \left(\partial_i u'_j\right) \,. \tag{7}$$

This equation has the generic form of a propagation operator on the left hand side, with source term on the right hand side. As will be seen in the next section, the r.h.s. can be neglected at small wavelengths and (7) then reduces to a standard propagation equation, with the effect of advection by the mean flow clearly visible in the $(\partial_t + \vec{u}_0 \vec{\nabla})$ term. If the flow velocity $\vec{u}_0$ were constant and uniform, Eq. (7) could have been obtained directly from the acoustics equations in a medium at rest using the Galilean invariance of the Navier–Stokes equations. Indeed, the transformation $((t \to t, \vec{x} \to \vec{x} - \vec{U}t, \vec{u} \to \vec{u} + \vec{U})$ just changes the time derivative ∂_t into $(\partial_t + \vec{U}.\vec{\nabla})$.

2 Geometrical acoustics

Here, the wavelength of the incident sound is assumed to be much smaller than the vortex core size. In this case, the right hand side of (7) can be neglected compared to the other terms. For example,

$$\frac{-2\rho_0 \left(\partial_j u_{0,i}\right) \left(\partial_i u'_j\right)}{\partial_t \left(\vec{u}_0 \vec{\nabla} \rho'\right)} \sim \frac{\rho_0 (u_0/a).(u'/\lambda)}{\nu_0 u_0 \rho'/\lambda} \sim \frac{\lambda}{a} \ll 1 \,. \tag{8}$$

Therefore, in the geometrical acoustics regime, the sound wave is locally advected by the vortex and the equation of propagation can be written as:

$$\left(\partial_t + \vec{u}_0 \vec{\nabla}\right)^2 \rho' - c^2 \Delta \rho' = 0 \,. \tag{9}$$

In the limit of small wavelengths, such an equation is usually treated introducing an eikonal function $\Psi(\vec{r}, t)$, and the fields are written, e.g., $\rho'(\vec{r}, t) = \rho'_0 \exp(ik\Psi(\vec{r}, t))$. In this case,the dispersion relation associated with (9) is

$$2\pi\nu_0 = ck + \vec{u}_0.\vec{k} \,, \tag{10}$$

where the wave frequency is $2\pi\nu_0 = -\partial_t \Psi$ and the wavenumber is $\vec{k} = \vec{\nabla}\Psi$. It leads to waves propagating at the (group) velocity:

$$\overrightarrow{V} = c\frac{\vec{k}}{k} + \vec{u}_0 \ . \tag{11}$$

To leading order in Mach number, the evolution of the direction of propagation $\vec{n}$ ($\equiv \vec{V}/V$) of acoustic rays along their paths, is then given by [5]

$$\frac{d\vec{n}}{ds} = -\frac{\vec{n} \times \vec{\omega}}{c} \ , \tag{12}$$

where $\vec{\omega}$ is the flow vorticity, and

$$\frac{\partial\phi(\vec{r})}{\partial k_i} = -k_i u_{0,i} \ , \tag{13}$$

(no summation rule) for the evolution phase ϕ along the ray.

For a known vorticity distribution, rays are then computed either by solving Eq. (9) directly (or the associated Helmholtz equation [10–12]) or by using a ray-tracing scheme based on Eqs. (11) and (13).

B Experimental results

The results reported in this section have been extensively detailed in Brillant et al. [19]. We summarize here the points that are connected with this review, focusing on the distortion of wavefronts after propagation through an isolated vortex.

1 Setup and measurement scheme

In order to generate an isolated vortex, we use the von Kármán geometry [13]. A strong large scale vortex is generated in the gap between two coaxial corotating disks [14]. Air is the working fluid. The disks, with diameter $2R = 20\,\text{cm}$, set $H = 27\,\text{cm}$ apart, are driven by DC motors at equal rotation rate $\Omega \in [10, 50]\,\text{Hz}$ kept constant with a PID feedback loop. This apparatus is placed at the center of an experimental room with walls, 3 m away, are covered with sound absorbing material. The flow is insensitive to these lateral boundaries. In order to increase the vortex intensity and stability, the rotating disks are fitted with a set of blades and covered with thin disks having a hole in their centers (Fig. 2). In this manner one can generate vortices with typical strength $\Gamma \sim 5\,\text{m}^2\,\text{s}^{-1}$ and core size $a \sim 3\,\text{cm}$. The vortex has a slow motion of precession [14, 15] about its axis. In our case, the vortex precesses with a period of about 1 s on a circular motion of radius $\sim 1.5\,\text{cm}$. This motion is only quasi-periodic: it can be monitored using a hot wire probe located roughly on the orbit of precession – see Fig. 2. The resulting velocity signal is used as a "clock" to compute an average of the pressure field, synchronous to the position of the vortex. The method, similar to boxcar, uses the adaptive pattern recognition algorithm described in [14]. One effect of this averaging mechanism is to wipe out the effect of the turbulent fluctuations (they are present because the Reynolds number of the vortex is of the order of 10^4, but they are incoherent with respect to the vortex motion).

Concerning the acoustic measurements, capacitive Sell-type transducers [16] (square, edge size $\Lambda = 16\,\text{cm}$) are used to insonify the vortex. The sound frequency is adjustable in the range $\nu_0 \in [7,\ 100]\,\text{kHz}$. The emitter is set at a distance equal to 66 cm from the disks rotation axis. The sound detector is a miniature B&K microphone (model 4138), located at an adjustable distance behind the vortex and whose position can be varied on a line parallel to the emitter, in 0.5 cm steps controlled by a step motor. Profiles of the acoustics fronts are obtained by recording long series of the acoustic field at each position of the microphone along a line perpendicular to the incident direction of propagation. The signal is then coherently averaged for a fixed location of the precessing vortex, using the clock given by the velocity measurement.

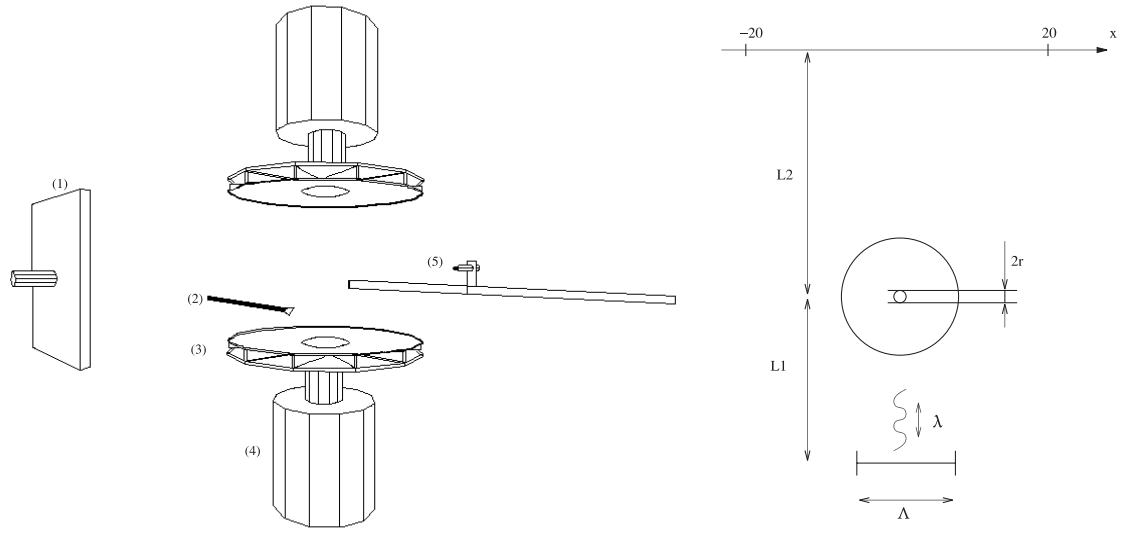

Fig. 2. Experimental setup. (1) Sell transducer used to insonify the vortex (set at $L_1 = 66$ cm). (2) Hot-wire probe to record a velocity clock signal. (3) Rotating disks (diameter $2R = 20$ cm, set 27 cm apart). (4) Driving motors (rotation rate adjustable in the range [10–50] Hz). (5) Miniature microphone (distance L_2 is adjustable). The disks rotation rates Ω are adjustable in the range 10 to 50 Hz

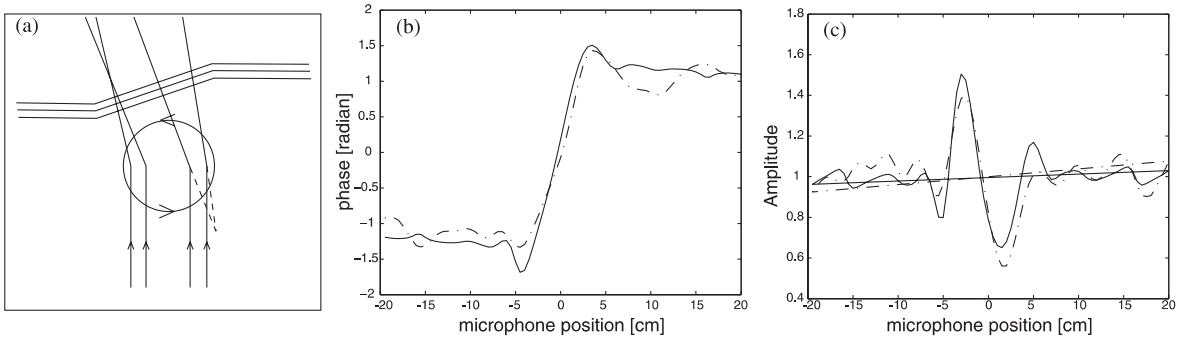

Fig. 3. (**a**) Schematics of wavefront distortion and ray path across the vortex, in the geometrical acoustics regime. The rays crossing closer to the center of the vortex meet a larger vorticity field and thus experience a stronger deviation (Eq. (12)). This produces a focusing effect (phase delay and amplitude increase) on one side and a defocusing effect on the other side (phase advance and amplitude decrease). (**b**) Typical phase measurement (*solid line*: simulation using a Rankine vortex profile; *dashed line*: experiment with $\Omega = 30$ Hz, $\nu_0 = 40$ kHz, $L_2 = 33$ cm). (**c**) Corresponding amplitude profiles

2 Results

From the evolution of the acoustic speed across the vortex, Eq. (11), and from the ray Eq. (12), one expects the behavior shown in Fig. 3a for the wavefronts propagating through the vortex.

The phase is advanced on the side where the velocity of the vortex has the same direction as the incident sound, and retarded on the other side. In addition, the deviation of the rays increases with the local amplitude of the vorticity field (Eq. (12)), i.e., for rays that impact closer to the vortex axis. As a result, a defocusing effect forms on one side of the vortex (where the phase is advanced) and a focusing effect develops on the other side. This is indeed observed in a typical measurement. Note that in order to incorporate the diffraction effect that results from the finite size of the transducers, the phase and amplitude profiles are computed normalized to measurements made in the absence of vortex flow.

Assuming axisymmetry, the phase jump across the vortex (Fig. 3b) is directly related to its circulation Γ [18]:

$$\Delta\Phi = \frac{\nu_o \Gamma}{c^2} \,. \tag{14}$$

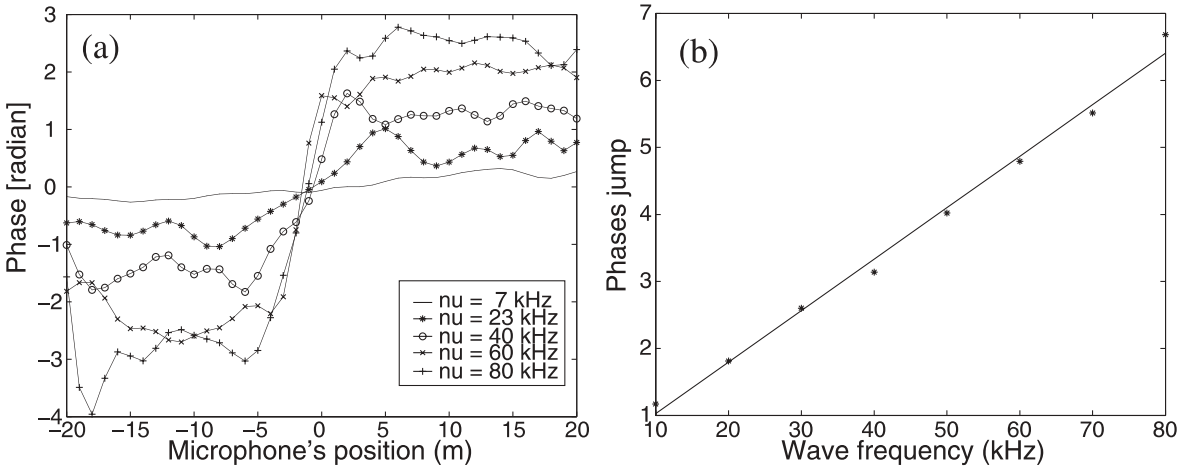

Fig. 4. (**a**) Phase profile and (**b**) magnitude of the phase jump, for increasing frequencies of the incident sound wave

(This result was also readily obtained from a dimensional argument [17].) Typical phase shifts in our experiment are of a few radians, in agreement with the above expression. Note that the phase jump can be re-expressed as a function of the flow Mach number $\Delta\Phi \sim (a/\lambda)M$. It shows the advantage of using gases in experiments of this kind, since higher Mach number can be achieved in gases. This is because the speed of sound in gases in roughly one order of magnitude lower than the speed of sound in liquids. In addition, as the density of gases is also lower, higher velocities can be achieved for a fixed power input of the flow driving device. As in the limit of small wavelengths, acoustic rays tend to bend proportionally to the local vorticity (Eq. (12)), and since the vortex vorticity distribution is a bell-shaped curve peaking on the vortex axis, one expects amplitude effects corresponding to focusing and defocusing effects (Fig. 3a,c). At the Mach numbers reached in air, amplitude variation as large as 50% of the reference amplitude can be observed.

We also note that the total angle θ of deflection of the acoustic rays may be estimated from Eq. (12). In our setup, we obtain $\theta \sim \arctan\left(\frac{\Omega.R}{c}\right) \sim 3.10^{-3}$, which is too small to be measured in our experiment where the maximum downstream distance L_2 is 1.2 m and the acoustic field is measured in 5 mm steps. The evolution of the phase profiles for several values of the incident sound wavelength is shown in Fig. 4a and the linearity of the phase jump with ν_0 is evidenced in Fig. 4b. Note here that a phase jump is observed to be proportional to the frequency outside the validity of the geometric approximation, as it is geometrically constrained by Eq. (14). Finally, the linearity of the phase shift jump both with the frequency of the incident sound and with the vortex strength (Eq. (14)) have been observed experimentally [19].

In the geometrical acoustics regime, the phase and amplitude profiles are easily computed numerically using Eqs. (12) and (13): straight rays are thrown from the Sell emitter in all directions and their phases are unwrapped along the rays. The amplitude and the phase of the wave are calculated in each measurement point by summing all the rays that hit this point. Of course, in order to perform an accurate simulation, one would need to know the actual vorticity distribution of the experiment. This is quite difficult in the von Kármán geometry of the experiment where the vorticity field differs appreciably with standard models such as Lamb, Rankine or Burger vortices. However some qualitative comparisons can be made. The solid curves in Fig. 3b,c have been obtained using the very simple Rankine vortex as a model (the vorticity is bounded, constant inside a core radius and zero outside). One observes that the width and amplitude of the phase jump are well accounted for: this is because they depend mainly on global parameters such as the vortex core size and overall strength. The amplitude variation in the wavefront is more sensitive to the actual vorticity distribution; one observes in Fig. 3c significant differences between the simulated and measured profiles.

We thus observe that, at short wavelength, there is a very good agreement between observations and the behavior that can be deduced by assuming the validity of geometrical acoustics. Measurements can actually be used to derive interesting vortex parameters such as core size, strength and the azimuthal velocity profile (under the assumption of axisymmetry [20, 21]).

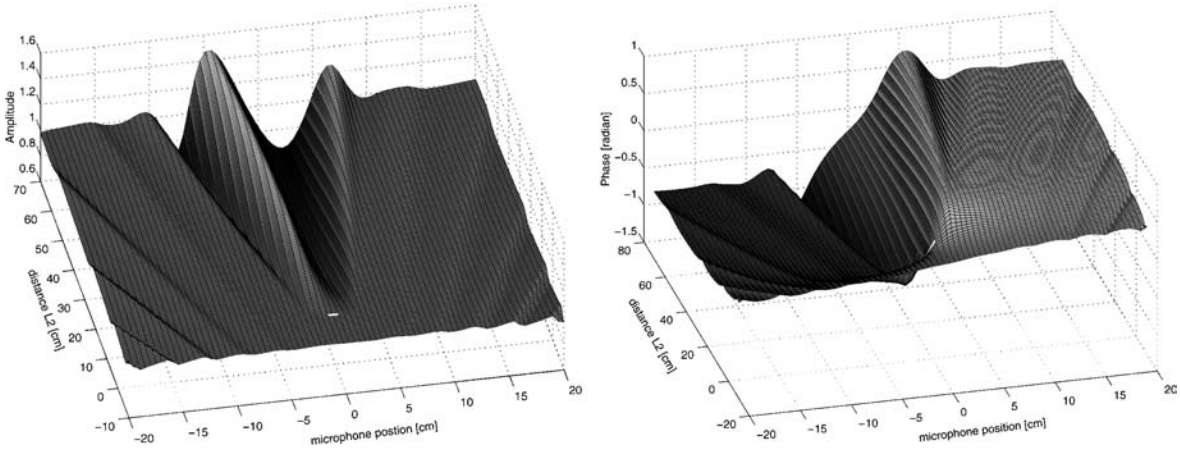

Fig. 5. Wavefront profiles, simulated over the experimental domain ($\Gamma = 1.4\,\mathrm{m}^2.\mathrm{s}^{-1}$, $a = 3\,\mathrm{cm}$, $\nu_0 = 40\,\mathrm{kHz}$)

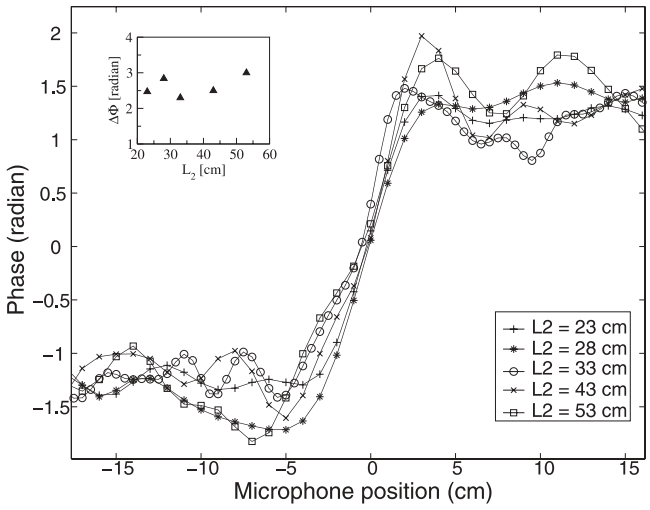

Fig. 6. Evolution of the phase profile with the distance of measurement L_2 to the vortex axis ($\Omega = 30\,\mathrm{Hz}$, $\nu_0 = 40\,\mathrm{kHz}$)

A typical evolution of the wavefronts after propagation through the vortex is shown in Fig. 5. One particular prediction of geometrical acoustics assumptions, which neglect scattering effects, is that the vortex mainly produces a "dislocation" in the wavefront. Once produced, this dislocation does not evolve with the distance downstream of the vortex. This is indeed observed experimentally, as shown in Fig. 6.

3 Transition to the scattering effects

The validity of the geometrical acoustics approximation breaks down when the wavelength of the incident sound reaches an order of magnitude of the vortex core size, or more precisely, when $ka \sim 1$. We have repeated the experiments described above, when the frequency of the incoming sound is lowered down to 7 kHz, i.e., for wavelengths up to 5 cm – larger than the vortex core.

We show in Fig. 7 the measured amplitude and phase variations downstream of the vortex for an incident sound at 15 kHz. In this case the parameter ka is equal to 8.3, so that the

measurement is clearly outside the geometrical acoustics domain. As a result, one observes clear deviation with respect to the case of small wavelengths, cf. Fig. 3c and the numerical prediction in Fig. 7. Both the amplitude and the phase have variations of order one over the entire range of microphone positions. The order of magnitude of the amplitude of the phase jump is still correctly given by the geometrical acoustics argument, but this is mainly due to the fact that the phase jump is locked to the circulation of the vortex [17]. The amplitude now has large oscillations, indicating that the angle over which the wavefront is disturbed is

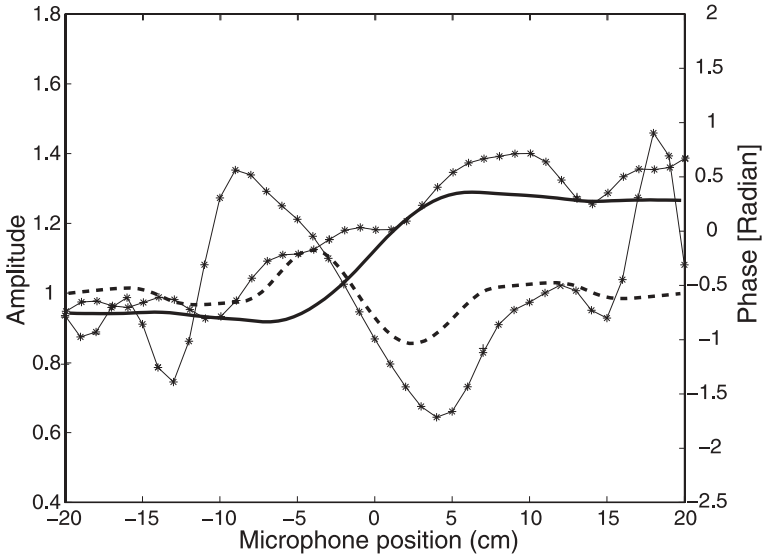

Fig. 7. Amplitude (⋆, dashed line) and phase (⋆, solid line) variations, for an incident sound at a frequency equal to 15 kHz, corresponding to a wavelength $\lambda = 2.3\,\mathrm{cm}$ ($ka \sim 8.3$). The symbols mark the experimental measurements, while the thick continuous lines are the results of numerical simulations using geometrical acoustics approximations

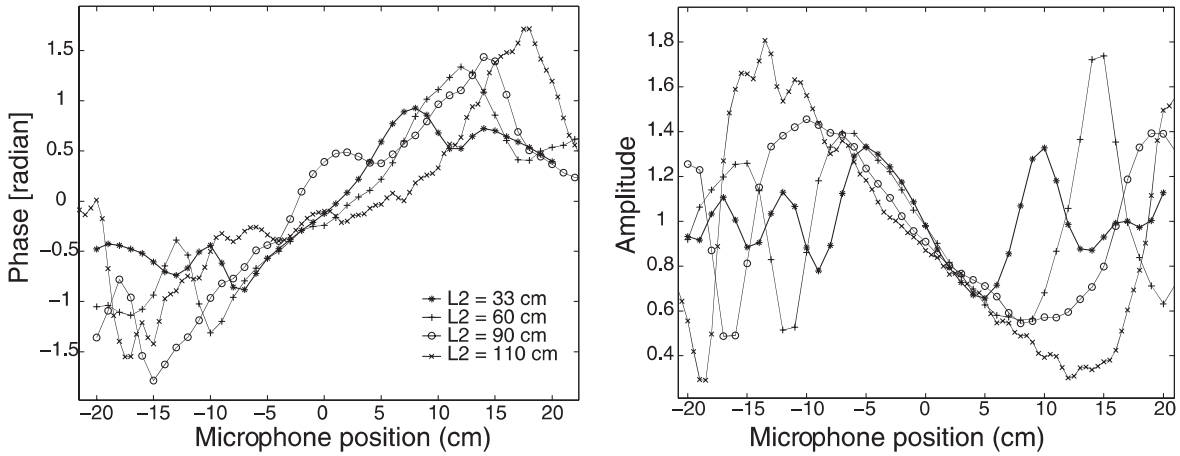

Fig. 8. Variation with the downstream distance in the scattering regime. ($\Omega = 30\,\mathrm{Hz}$, $\nu_0 = 20\,\mathrm{kHz}$)

greatly increased compared to the geometrical acoustics argument. Overall, these effects are clear indications of diffraction phenomena, i.e., of the scattering of the incident sound by the vortex structure.

Another distinctive feature of the scattering effects is that the wavefront varies strongly with the distance downstream of the vortex, as shown in Fig. 8. One observes a linear increase of the central region with the distance L_2. It yields an estimate of the main scattering lobe, $\Delta\theta \sim 19$ deg for the measurement at 20 kHz. This observation is in very good agreement with recent direct numerical simulation of the full problem (propagation and scattering effect) in which the r.h.s. of Eq. (7) is taken into account [22, 23].

In order to further test the scattering by vortices, one should rather use vorticity distributions that are spatially well controlled. This is the case of the von Kármán vortex street that develops in the wake of a cylinder, which will be discussed in the next section.

III Scattering

A Theoretical background

The geometry under consideration is typical of a scattering experiment: an incident (plane) sound wave impacts a flow with a vorticity distribution $\vec{\omega}(\vec{r}, t)$. Acoustic transducers are used to record the scattered wave at

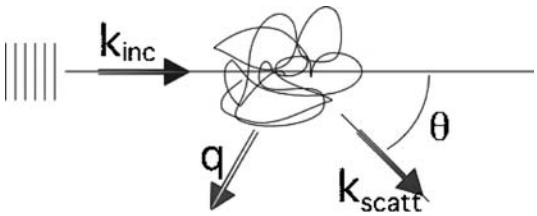

Fig. 9. Schematics of a scattering experiment. $\vec{k}_{\rm inc}$ is the wave vector of the incident sound, $\vec{k}_{\rm scatt}$ is the wave vector in the direction of the scattered sound and $\vec{q} = \vec{k}_{\rm scatt} - \vec{k}_{\rm inc}$ is the scattering wave vector. The flow is bounded and the measurements are made in the far-field region

an angle with the incident direction, far away from the flow (Fig. 9). Physically, the mechanism is as follows: the incident sound advects the vortices in the flow, which then act as secondary sources of sound (nonstationary vortices are sources of sound in much the same way as accelerated particles radiate electromagnetic waves). This "stimulated" emission is then detected by the acoustic receivers. Analytically, in the case of a bounded flow, one would like to formulate the problem under the generic form:

$$\frac{1}{c_0^2}\partial_{tt}p^s - \Delta p^s = \text{source}\,, \tag{15}$$

where c_0 is the velocity of sound in the undisturbed medium in which the acoustic transducers are located. The source term involves the velocity gradients in the flow and the incoming sound wave. It comes from the nonlinear terms in the Navier–Stokes equations, which couple the sound and vorticity hydrodynamics modes [24].

Taking the divergence of the momentum equation and the time derivative of the mass conservation equation, one obtains the exact equation:

$$\frac{1}{c_0^2}\partial_{tt}\rho - \Delta p = \text{div}\left(-\vec{u}\,\partial_t\rho + \rho\big(\vec{u}.\vec{\nabla}\big)\vec{u}\right)\,. \tag{16}$$

To transform it into a scattering equation such as (15), (1) one writes all the fields as the sum of flow and sound contributions, e.g. $\vec{u} = \vec{u}_0 + \vec{u}^s$, with $\rho^s = p^s/c_0^2$, (2) the r.h.s. is developed in order of Mach number contributions, with the condition that the scattering wavenumber is close to a nonzero Fourier component of the vorticity field, which means that the sound wavelength is on the order of the characteristic length ℓ of the velocity gradients inside the flow: $\lambda \sim \ell$. In a first Born approximation (single scattering regime, calculation of the scattered sound in the far field), the acoustic field in the source region is taken to be equal to the incident sound field, and to the leading order Mach number, (16) leads to [9, 25]:

$$\frac{1}{c_0^2}\partial_{tt}\rho - \Delta p = \underbrace{-\rho_0\,\text{div}\left(\vec{u}^{\rm inc}\times\vec{\Omega}_0\right)}_{s_1} + \underbrace{\partial\left(\vec{u}_0.\vec{\nabla}\rho^{\rm inc}\right) - \rho_0\Delta\left(\vec{u}^{\rm inc}.\vec{u}_0\right)}_{s_2}\,. \tag{17}$$

The first term corresponds to the direct scattering by the vortices in the flow. In the far field, the scattering contributions from the source terms s_1 and s_2 are proportional: $p_2^{\rm scatt} = -p_1^{\rm scatt}/(1-\cos\theta)$, if θ is the scattering angle (Fig. 9). A solution for (17) in three-dimensional unbounded space has been obtained by Lund et al. [9]:

$$p^{\rm scatt}(\vec{r},t) = p^{\rm inc}\,\frac{\cos\theta\sin\theta}{1-\cos\theta}\,\frac{i\pi^2\nu_0}{c_0^2}\,\frac{e^{i(\nu r/c_0-\nu_0 t)}}{r}\omega_\perp(\vec{q},t)\,. \tag{18}$$

In the above expression ν_0 is the frequency of the incoming sound wave, $\vec{q}$ is the scattering wave vector in the direction θ. $\omega_\perp$ is the vorticity component perpendicular the scattering plane defined by $(\vec{k}_{\rm inc}, \vec{k}_{\rm scatt})$. The following remarks are important both theoretically and in regards to experimental applications:

- As expected in the Born formalism, the scattered field is proportional to the Fourier transform of the field of scatterers. Analogously to electromagnetic theory one can say that the incident sound waves advects the vortices of the flow, which then emit sound, but this simple argument is somewhat misleading because it ignores the contribution from the source term s_2 in (17). Actually vorticity-free flows, such as a potential flow, would scatter sound, but this contribution is at a higher order in Mach number and thus is not taken into account when the flow vorticity is nonzero [23].

- Only the component of the vorticity field perpendicular to the scattering plane (defined by $(\vec{k}_{\rm inc}, \vec{k}_{\rm scatt})$) is probed. The reason is that an unsteady vortex generates longitudinal velocity variations only in a direction perpendicular to its axis [26].
- The amplitude of the scattered sound is proportional to the Mach number of the flow M. Considering the very rapid decrease of the (quadrupolar) angular term, the experimental scattering cross section is very weak, typically about 10^{-4} or less. The sound scattered by stationary vortices is lost in the experimental noise. However, the sound scattered by vortices moving with a characteristic velocity $\vec{U}$ is Doppler-shifted to frequency $\nu_0 + \vec{q}.\vec{U}/2\pi$, which makes it clearly recognizable, for example, in the Fourier spectrum of the measured acoustic pressure.
- There is no backscattering. This is not the case for the scattering by temperature fluctuations, for which the scattering is dipolar [27, 28]. This feature could be used to distinguish between temperature and vorticity contributions in the study of laboratory flows. Note also that the divergence of the scattering amplitude in the forward ($\theta = 0$) direction traces back to a problem in the first Born approximation itself [23, 29].

B Scattering by the von Kármán vortex street

The simplest configuration to use to study a scattering phenomenon is the diffraction grating experiment. In our case, the idea is to test the scattering by a regular array of parallel vortices [31–34]. This arrangement, known as the von Kármán vortex street, is produced in the wake of a cylinder when the Reynolds number of the flow (based on cylinder diameter and upstream speed) exceeds approximately 45 [30]. In this case an array of alternate vortices is formed downstream of the cylinder. Three major characteristics of the scattering of sound by vorticity can be tested in this configuration: (1) the dependence on the orientation of the vortices with respect to the scattering plane, (2) the proportionality with the amplitude in Fourier space of the vorticity field, and (3) the main forward contribution of the scattering.

1 Experimental setup

The experiment described here is that of Baudet and coworkers [32]. A low-speed wind tunnel, with a very low turbulence level is used to generate the vortex street in the wake of a cylinder [32]. The diameter of the cylinder and the upstream velocity are adjustable. Above the critical Reynolds number, a double row of vortices with equal strength and opposite sign is formed in the wave of the cylinder [30] (Fig. 10). The spacing b between vortices in each row is equal to 5.4 times the cylinder diameter and the array moves downstream with a speed U equal to 91% of the mean velocity (lower than the mean velocity due to the mutual influence of the vortices).

Reversible acoustic transducers (diameter $\Lambda = 8$ cm) of the Sell type [16] are used to generate the incoming sound and to detect the scattered wave. The characteristic velocity of the sound wave is 1 cm/s, much

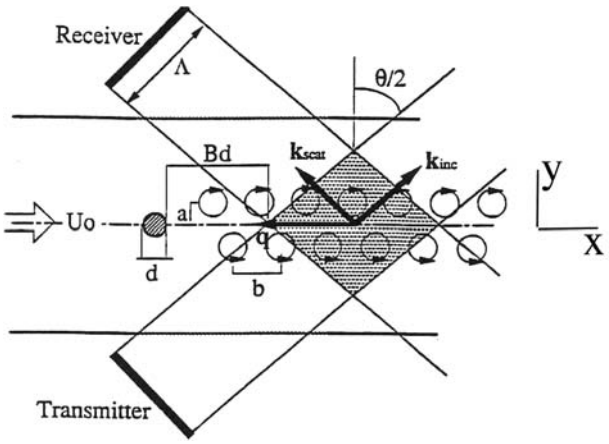

Fig. 10. Scattering from the von Kármán vortex street; schematics of the experimental setup. U_0 is the upstream parallel flow speed, b the streamwise separation between two vortices of like-signs and a the span-wise separation between the two rows of vortices of opposite strength $\pm\Gamma$; $\vec{k}_{\rm inc}$ and $\vec{k}_{\rm scatt}$ are, respectively, the incident and scattering wave vectors at an angle θ from one another. The Sell transducers are squares with side dimension $\Lambda = 16$ cm. Figure from [32]

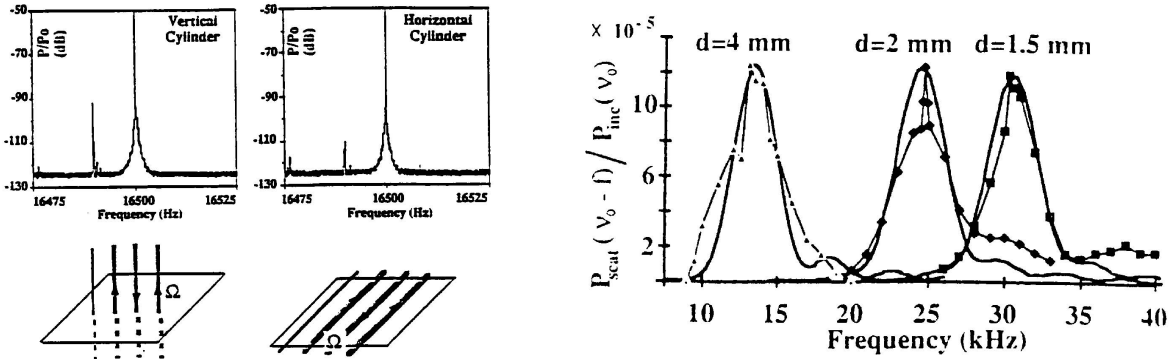

Fig. 11. Scattering from the von Kármán vortex street. *Left*: Fourier spectrum in time of the signal at the receiver when the cylinder is set either perpendicular (labeled vertical cylinder) or parallel to the scattering plane (labeled horizontal cylinder). *Right*: variation of the scattered amplitude with the frequency of the incoming sound wave ν_0, for three different wakes produces at the same Reynolds number using cylinders diameter 1.5, 2 and 4 mm. The resonance frequencies are in the same ratio. Figure from [32]

smaller than the typical velocities in the fluid flow (of the order of 60 cm/s). Incident sound frequencies are adjustable in the range $\nu_0 \in [10, 100]$ kHz, corresponding to wavelength $\lambda \in [30, 3]$ mm. In the experiment, it is more convenient to vary the scattering wavenumber by varying the frequency of the incident sound at a fixed scattering angle than to vary the scattering angle (as is traditionally done in optics).

2 Results

With an incoming wave at frequency ν_0, the vorticity distribution is probed at wavenumber $q = 4\pi\nu_0 \sin\theta/c = 4\pi \sin(\theta/2)/\lambda$. A strong scattering signal is expected when one adjusts it to be equal to $2\pi/b$, where b is the spacing between vortices (resonance condition). Figure 11(left) shows a spectrum in time of the sound detected by the receiver when the resonance condition is met. One observes a large spectral line at the frequency of the incident sound, mainly due to echoes and reflection over walls and objects in the laboratory. To its left is a peak due to the scattering by the vortices. It is at a different frequency than the incident sound because of the Doppler shift resulting from the downstream motion of the vortex array, and the shift is negatively shifted because in the setup the scattering wave vector direction is opposite to the averaged flow velocity (Fig. 10). When the cylinder is rotated by $\pi/2$ so that the vortex street now lies within the scattering plane, one observes (Fig. 11 (left)) that the scattered amplitude is reduced by over an order of magnitude (the remaining signal is due to the fact that the vortices in the street have a 3D structure). This comparison shows the sensitivity to the orientation of the vorticity, as predicted by Eq. (18).

The resonance condition can be tested by varying the frequency of the incident sound. Figure 11 (right) shows the evolution of the amplitude of scattering peak as ν_0 is varied. Using cylinders of different diameters, we have verified that the maximum occurs for $\nu_0 = c/2b \sin(\theta/2)$ as expected, i.e., when the Bragg condition is met. Another noteworthy feature is that their is no scattering signal at twice the resonance frequency. This is because the vortices in the street have alternating signs, so that if $q_r = 2\pi/b$ is the resonant wavenumber, there is no Fourier component at $2q_r$. Actually a very good fit of the experimental data is obtained (Fig. 11(right)) – if one models the vortex street by a simple array distribution: $\Omega_z(x, y, t) = \sum_{n>0}(-1)^n \Gamma\delta(x - nb - Ut, y + (-1)^n a)$. Several additional features have been checked in this experimental configuration [32–34]. The angular dependence of the scattering amplitude is for $\theta > 0$ correctly given by Eq. (18), which confirms the quadrupole nature of the scattering by vortices.

C Scattering by vorticity filaments in fully developed turbulence

The above results show the possibility of a spectral measurement of vorticity. It is therefore of interest to test the technique on more complex vorticity distributions, such as can be found in turbulent flows. In particular,

the possibility of developing intense vorticity concentrations in turbulent flows has been the subject of many studies. Observations (numerical and experimental) indicate the presence of elongated vorticity tubes whose lengths are on the order of the flow size and whose core is a much smaller size – hereafter they are referred to as filaments. The main issues have been (1) a fluid mechanics one in regards to the existence of coherent vorticity filaments in spatially fluctuating flows such as three-dimensional turbulence [36], and (2) a statistical physics one in regards to the possible role of filaments in deviations from Kolmogorov scaling laws [37, 38]. A comprehensive discussion of these features is well outside the scope of this report, which aims to show how the use of acoustic scattering helped clarify some issues [39]. Specifically, vorticity filaments in laboratory flows were (and are) observed with one of three methods: (1) in a liquid seeded with gas, the bubbles are drawn to the center of the filaments core [40] allowing for visualizations of the filaments, (2) as they sweep the walls of the flow, filaments produce pressure drops which can be detected by a pressure probe [41], (3) localized velocity probes (such as a hot-wire anemometer) can record a trace of the sweeping of a filament past the probe [38, 42]. However none of these methods yield direct access to the vorticity field in the bulk of the flow, and questions remain open as to bulk filament statistics and size.

We stress here that the use of ultrasound as a probe of turbulence in atmospheric flows traces back to the pioneering analytical work of Obukhov and measurements by Kallistratova and coworkers [43–45]. The results reported here come from a study by Dernoncourt et al. [39].

1 Experimental setup

The test flow is again produced in a von Kármán setup as shown in Fig. 12. Two ac motors drive smooth disks of radius $R = 9.9\,\mathrm{cm}$ at a constant rotation rate. The disks spin in counter-rotation in order to generate turbulence. The enclosing cylindrical vessel has a volume of 5.5 l and is cooled using constant temperature bath/circulators and thus kept at a constant temperature. The rotation frequency ($f_{\mathrm{rot}} = 1/T_{\mathrm{rot}}$) is varied from 650 to 1500 rpm, and three different fluids are used (F1: pure water), (F2: mixture water/glycerol 28% mass fraction), (F3: mixture water/glycerol 48% mass fraction). Reynolds numbers, $Re = 2\pi R^2 f_{\mathrm{rot}}/\nu_v$ (ν_v is the kinematic viscosity of the fluid), ranging from 1.5×10^5 to 1.5×10^6 are achieved. In these conditions one reaches a maximum value for the Taylor based Reynolds number of the order of $R_{\lambda_T} \sim 400$, with $\lambda_T \sim 100\,\mu\mathrm{m}$.

The sound emitter (Em) and receiver (Rc) are reversible MATEC piezoelectric broad band transducers, located in a plane perpendicular to the rotation axis. Pairs of transducers with central frequencies of 2, 5 and 10 MHz are used. The flow is thus probed in the frequency range [1, 15] MHz. The scattering angle is fixed at 60° in the forward direction. The scattered wave is monitored using an HP3588A – 150 MHz spectrum analyzer. The echoes and stationary components that are at the frequency ν_0 of the incident sound are filtered out numerically from the signal detected by the receiving transducer (these components are due to reflections of the incoming sound on the flow walls and to crosstalk of the transducers through propagation through the flow vessel and electromagnetic radiation). Starting with a sampling in a frequency band 20-kHz wide centered on ν_0, this filtering reduces the effective time resolution of the scattered amplitude to 1 ms. This time is much smaller than the life-time of filaments, as observed in visualization and pressure measurements (about

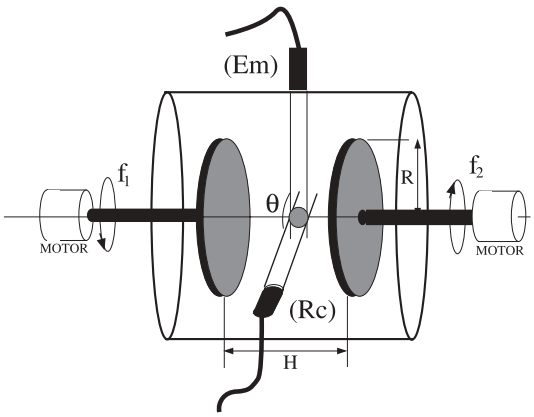

Fig. 12. Experimental setup. The 19.8-cm diameter smooth disks are 10 cm apart; the external vessel has an internal diameters of 20 cm and a length of 20 cm for a volume of fluid of about 5.5 l. θ is the scattering angle between sound emitter (Em) and receiver (Rc). To avoid cavitation effects, the pressure in the vessel may be raised up to 1.8 atm. The vorticity component parallel to the rotation axis is measured

100 ms), however it is too large to probe the internal dynamics of the filaments, which have a turnover time of the order of the Kolmogorov dissipative time scale (about 80 μs here).

2 Results

We first recall that the scattering amplitude in the case of a localized vortex has been calculated by Ferziger [46] for a rectilinear Gaussian vortex of core size r_0 and intensity Γ_0:

$$v(r) = \frac{\Gamma_0}{2\pi r}\left(1 - e^{-r^2/r_0^2}\right),$$

showing that the scattering cross section $S(q,\theta)$ peaks at $q_{\max} = \frac{1}{2r_0 \sin(\theta/2)} = 1/r_0$, since $\theta = 60°$ is used in the experiment.

Let us first consider a measurement in which the incident sound frequency is tuned in a band such that the scattering wave vector has values outside length scales where filaments are expected. A short-time power spectrum of the scattered sound has the typical feature shown in Fig. 13a. Around the large peak at ν_0 (echoes, etc.) one observes a broad spectrum corresponding to the scattering by the vorticity of the turbulent flow at wavenumber q. Its fluctuations in time, obtained after filtering the central line at ν_0 are shown in Fig. 13c. As expected they are very close to Gaussian [43–45, 47, 48].

Now, the sound frequency can be tuned to a band corresponding to the filaments core size. Short-time Fourier spectra of the scattered acoustic signal show very intense bursts, as displayed in Fig. 13b. These

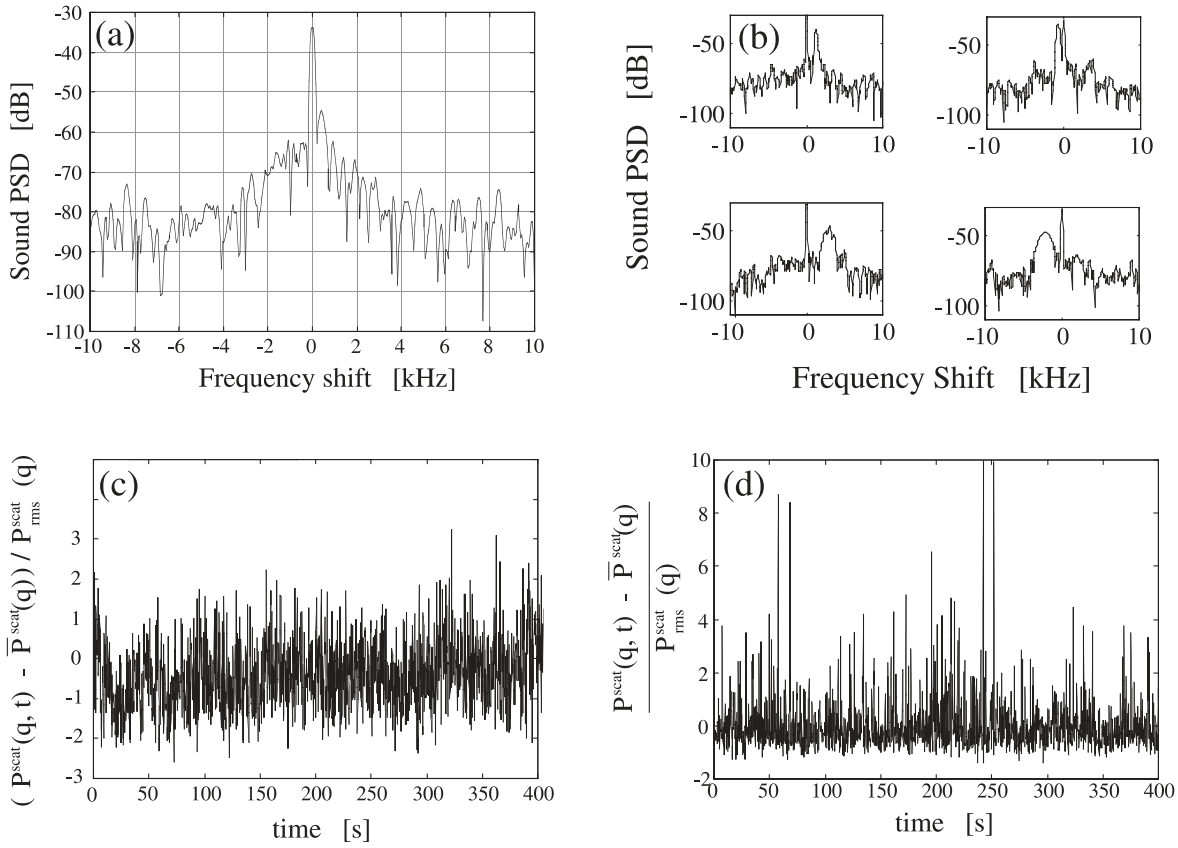

Fig. 13. (**a**,**b**) Short-time power spectral density of the pressure measured by a transducer at a scattering angle of 60 degrees. The x-axis represents the Doppler shift, so that 0 corresponds to ν_0. The fluid is pure water and the disks are counter-rotating at 1000 rpm. In (**a**) $\nu_0 = 6$ MHz; in (**b**) $\nu_0 = 10$ MHz. (**c d**) Time evolution of the scattered sound amplitude obtained after filtering of the spectral component at ν_0 in spectra shown above – $P^{\rm scat}(q,t) \propto \int_{|f|>\Delta} df\, P^2_{\rm scat}(\nu_0 + f)$. (**c**) corresponds to $\nu_0 = 6$ MHz and (**d**) to $\nu_0 = 10$ MHz

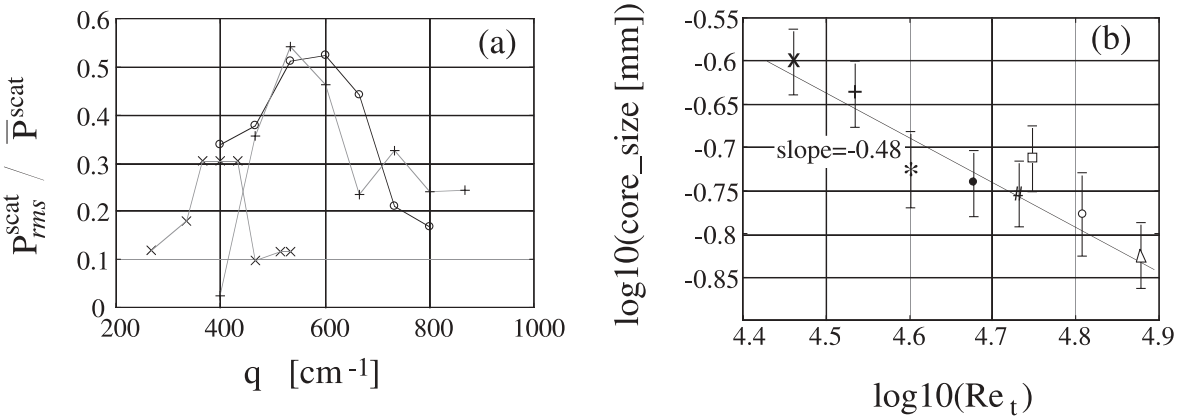

Fig. 14. (**a**) Scattering amplitude fluctuation level vs. incoming sound frequency, for three different Reynolds numbers. *Solid line* (*circles*): pure water at 1000 rpm, $Re \sim 10^6$; *dashed line* (*plus sign*): water and glycerol (28% in mass) at 1000 rpm, $Re \sim 0.7 \times 10^6$; *dash-dotted line* (*cross*): water and glycerol (48% in mass) at 650 rpm, $Re \sim 10^5$. (**b**) Filaments core size measured from curves similar to (**a**), as a function of the turbulent Reynolds number. (×): F3, 650 rpm; (+): F3, 1000 rpm; (∗): F2, 650 rpm; (•): F2, 1000 rpm; (#): F2, 1500 rpm, (□): F1, 650 rpm; (○): F1, 1000 rpm; (△): F1, 1500 rpm. The solid line is a $Re_t^{-\alpha}$ fit, with $\alpha = 0.48$

burst are highly intermittent (they follow Poisson statistics [39]). The corresponding time fluctuations of the scattered amplitude (Fig. 13d) are highly non-Gaussian. One observes, with a significant probability, events larger than 10 standard deviations.

When the frequency ν_0 of the incoming sound is varied, one observes a resonance of the fluctuation level $P_{rms}^{\mathrm{scat}}(q)/\overline{P}^{\mathrm{scat}}(q)$, where *rms* refers to the standard deviation and the overbar denotes time averaging. This is shown in Fig. 14a for flows at different Reynolds numbers. In each case the maximum of the curve defines a characteristic scale for the detection of the filaments. Note that the resonance is a shallow one, showing that filamentary vorticity structures exist with a wide range of core sizes.

Using a mixture of water and glycerol it is possible to cover a large range of integral Reynolds numbers. The variation of the filaments core size (measured from resonance peaks) with the integral Reynolds number is displayed in Fig. 14b. It varies as $Re^{-0.48}$. This behavior is very close to $1/\sqrt{Re}$, indicating that vorticity filaments in turbulent shear flows have a core size on the order of the Taylor microscale.

IV Further hydrodynamics measurements using acoustics

The studies presented in this last section are less directly concerned with the problem of sound and vorticity interactions. However they have generated new promising experimental techniques that use ultrasound to probe fluid flows. Their main advantages are to be nonintrusive and to have potential applications in nontransparent, high-temperature and/or corrosive fluids.

A Time-resolved Fourier dynamics

Scattering experiments can be performed using multiple pairs of acoustic transducers, so that it is possible to probe simultaneously the vorticity field at several wave vectors $\vec{q}_1$, $\vec{q}_2$, etc. This is a very interesting possibility because it allows one to study nonlinear transfers directly in Fourier space. For example, the nonlinear term $(\vec{u}.\vec{\nabla})\vec{u}$ of the Navier–Stokes equation governs the dynamics of turbulence. In Fourier space, it corresponds to triadic interactions $\left(\vec{u}(\vec{q}_1,t), \vec{u}(\vec{q}_2,t), \vec{u}(\vec{q}_2,t)\right)$, with $\vec{q}_1+\vec{q}_2+\vec{q}_3=\vec{0}$, and very little is known about them from direct experimental measurement. We report here results obtained by Baudet and coworkers [49], using jet turbulence as a test flow.

The measurement is set to follow the correlations in time of the enstrophy at two wavenumbers $\vec{q}_1$ and $\vec{q}_2 = \vec{q}_1 + \delta\vec{q}$ – see Fig. 15. The correlation function is estimated using reduced interference time-frequency

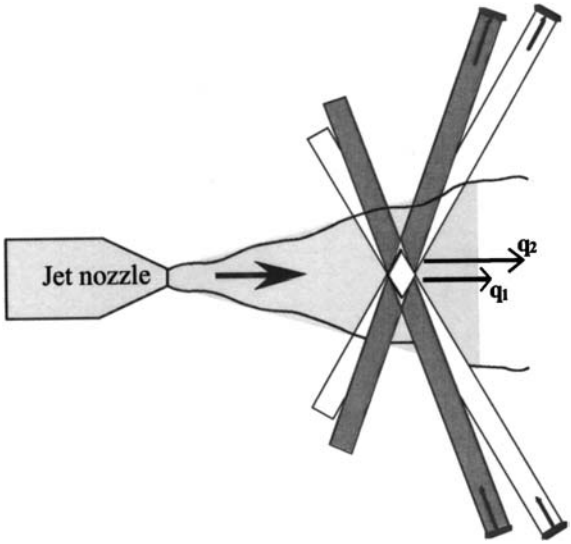

Fig. 15. Experimental setup, with two channels of acoustic scattering. The region under analysis is at their intersection. The first pair of acoustics (emitter-receiver) is set to probe the scattering wave vector $\vec{q}_1$ as in Figs. 9 and 10, while the second pair is tuned to $\vec{q}_2 = \vec{q}_1 + \delta\vec{q}$. The jet flow has a turbulent Reynolds number $R_\lambda \sim 600$ produced by air emerging at 60 m/s from a 5 cm circular nozzle

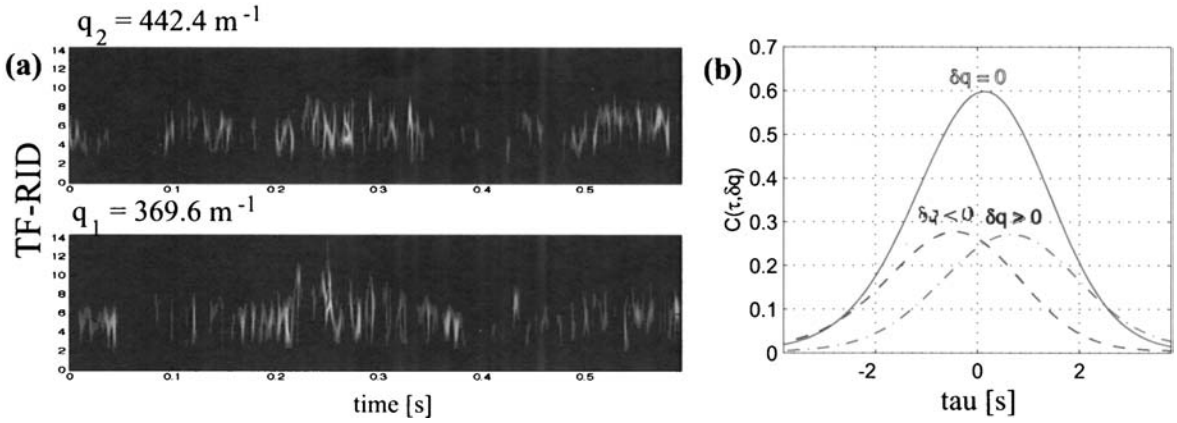

Fig. 16. (**a**) TF-RID distributions for each channel, which probe the flow, respectively, at $q_1 = 369.6\ \mathrm{m}^{-1}$ (emission at 20 kHz, scattering angle equal to 60 degrees) and $q_1 = 442.4\ \mathrm{m}^{-1}$ (emission at 29.4 kHz, scattering angle equal to 40 degrees), both well within the inertial range. (**b**) Correlation $C(\tau, \delta q)$ for three values $\delta q = 0, 0.2, -0.2\ \mathrm{cm}^{-1}$. Figures from reference [49], courtesy of C. Baudet

distributions (RIDs) that have been introduced [50] for the analysis of nonstationary signals:

$$C(\tau, \delta q) = \left\langle \frac{\int df\, \mathrm{TFR}_q(t, f)\mathrm{TFR}_{q+\delta q}(t+\tau, f)}{\int df\, \mathrm{TFR}_q(t, f)^2 \int df\, \mathrm{TFR}_{q+\delta q}(t+\tau, f)^2} \right\rangle , \tag{19}$$

where $\mathrm{TFR}_q(t, f)$ is the RID frequency distribution at time t of the acoustic signal at wavenumber q. Two examples of TF-RID signals and the averaged correlation function $C(\tau, \delta q)$ are shown in Fig. 16. When $\delta q = 0$, both channels probe the same wavenumber and the correlation between the two signals is a maximum. When $\delta q \neq 0$, the maximum is reached with a time delay τ, which evolves monotonously from negatives values (for $\delta q < 0$) to positive values (for $\delta q > 0$). This observation constitutes the first experimental evidence of the development in time of a turbulent cascade from large ($\delta q < 0$) scales to smaller ($\delta q > 0$) scales.

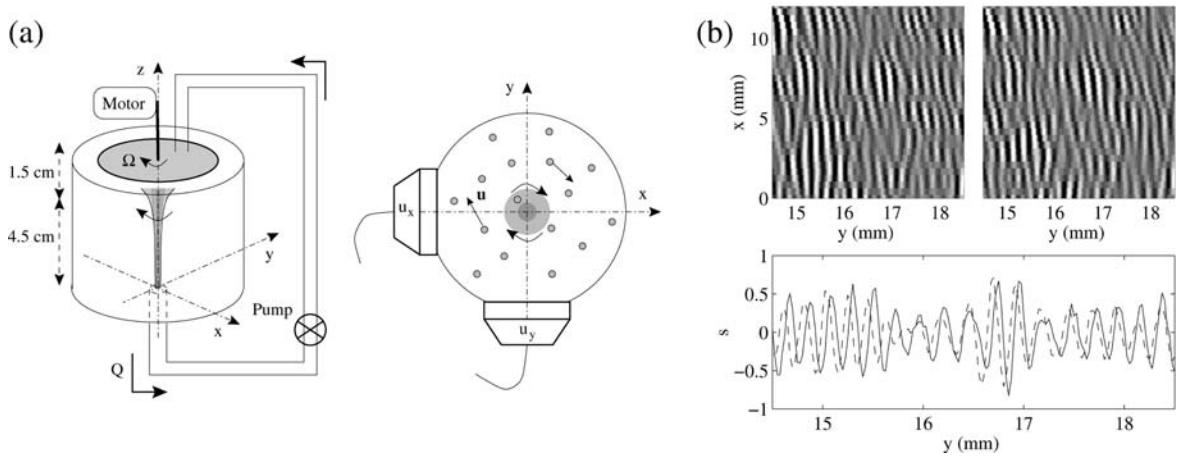

Fig. 17. (**a**) Experimental setup. An axial vortex is produced inside a cylinder filled with water by the rotation of the upper plate and pumping of fluid at the bottom (both adjustable). Transducer arrays (64 elements operating at 3.5 MHz) are located in a transverse plane, each measuring one component of the velocity field. The contrast agent is made of air bubbles imbedded in a galactose membrane, with a diameter ranging from 1 to 10 μm. (**b**) Two successive speckle $s_t(x, y)$ and $s_{t+T}(x, y)$ images taken at a rate $1/T = 3$ kHz. The lower figure shows cross sections of s_t and s_{t+T} at $x = 6.5$ and on 4 mm. Figure from [51], courtesy of S. Manneville

B Speckle interferometry

The acoustic technique presented so far leads to global measurements: sound transmission yields integral information over the acoustic ray path and the scattering techniques measure the spatial Fourier transform of the vorticity field over the measurement area. Local velocity measurements have been recently obtained by Manneville, Sandrin and Fink by combining classical ultrasonic Doppler velocimetry with echographic techniques in a promising measurement technique they have named ultrasonic speckle interferometry [51, 52]. Like optical particle tracking velocimetry (PTV), it yields a resolved velocity measurement in real space, but it is not limited to the study of transparent fluids.

The flow must be seeded with a homogeneous distribution of scatterers (small construct particles). Linear transducer arrays are used to record the speckle signal backscattered by the particles at a high frame rate (about 5 kHz). Speckle data analysis then yields the component of the velocity field in the direction of ultrasound propagation.

We briefly report on their application of this technique to the determination of the velocity field in a stretched vortex, in the geometry shown in Fig. 17a. After a 1 μs pulse (three acoustic periods), the transducers in the array record the backscattered signal, which results from the interference of the waves from each of the scatterers. A scatterer located at (x, y) generates a pressure contribution on an array element at x_0, at time $t = y + \sqrt{y^2 + (x - x_0)^2}/c$ and a speckle image is thus formed as the sum of the contribution at time t from all the scatterers:

$$s(x, y) = \sum_{x_0} p(x_0, t(x_0, x, y)) \ . \tag{20}$$

(In the equation above one may also include an apodization factor to account for the directivity of the transducers.) From the intercorrelation of two successive speckle images, s_t and s_{t+T}, one computes the displacement of the scatterers during the time interval T. For example, one clearly observes in Fig. 17b that the speckle pattern has moved to the left by about 0.05 mm in the 0.33 ms interval, so that $u_y \sim -15$ cm/s. When this procedure is repeated with two transducer arrays at a right angle to each other, one obtains a complete measurement of the vortex velocity field in a plane perpendicular to its axis. In the case of the stationary vortex produced in this setup the fields can be time-averaged and one finally obtains the vorticity and velocity distributions shown in Fig. 18. A maximum vorticity of about 250 rad/s is reached for a disk rotation speed of 3 rad/s, showing that the stretching induced by the pumping amplifies the vorticity by a factor of almost one hundred! The velocity profile is very close to that of a Burgers vortex to which a very small solid body rotation is superimposed.

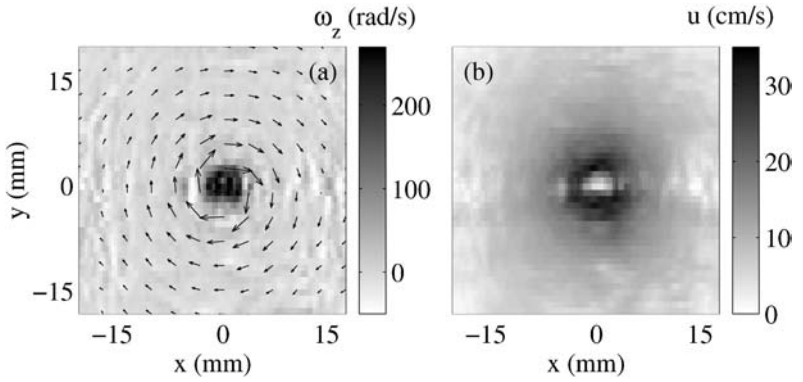

Fig. 18. (**a**) Vertical vorticity $\omega_z(x, y)$ and velocity vector $(u_x(x, y), u_y(x, y)$ deduced from the speckle images. (**b**) Modulus of the horizontal projection of the velocity vector

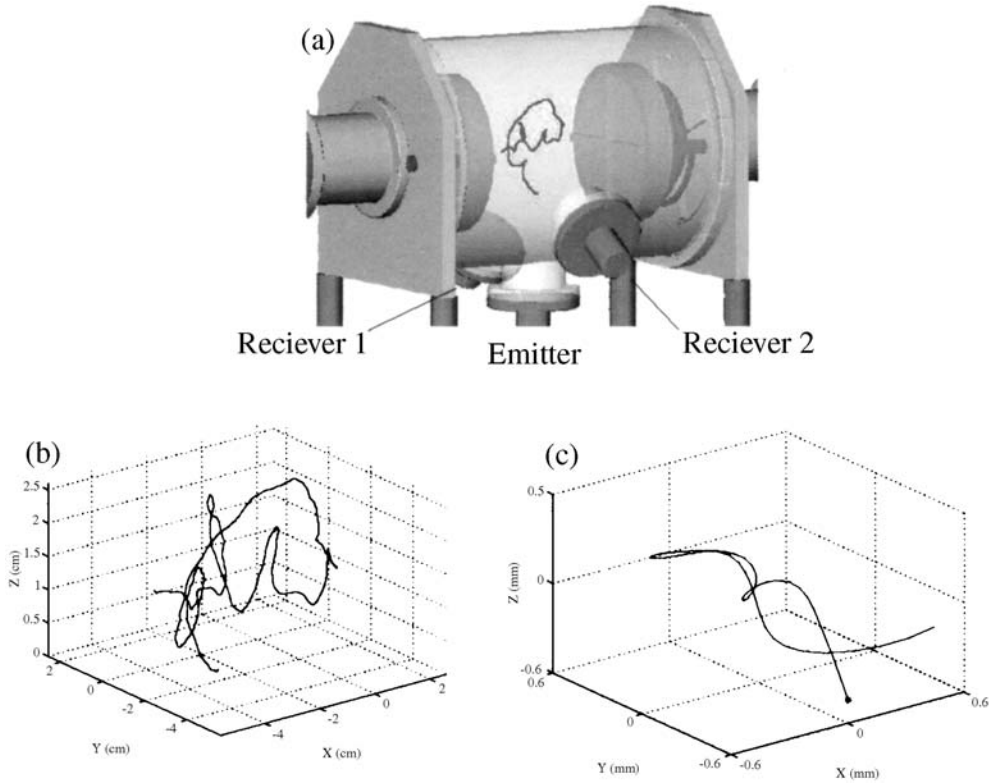

Fig. 19. (**a**) Experimental setup. A von Kármán swirling flow is generated inside a cylinder by counter-rotation at $\Omega = 7$ Hz of two disks with radius $R = 9.5$ cm, fitted with eight blades of height 0.5 cm and set 18 cm apart. The turbulent Reynolds number of the flow is $R_\ell = u_{rms}\ell/\nu = 740$. (**b**) Example of particle trajectory. (**c**) Small portion of a trajectory when the particle winds around a vorticity filament

C Lagrangian particle tracking

Again using arrays of acoustic transducers, a tracking method has been recently introduced to obtain independent measurements of the position and velocity of single particles in complex flows [53]. The idea is to obtain Lagrangian measurements of particle motion in complex flows. The method is based on the principle of a continuous Doppler sonar. The flow volume is continuously insonified with a monochromatic ultrasound and one tracer particle is introduced into the flow. The sound scattered by the tracer particle is detected by two transducer arrays to obtain a measurement of both the particle position, by direct triangulation, and the particle velocity, from the Doppler shift of the scattered sound. Indeed, for an incoming sound with fre-

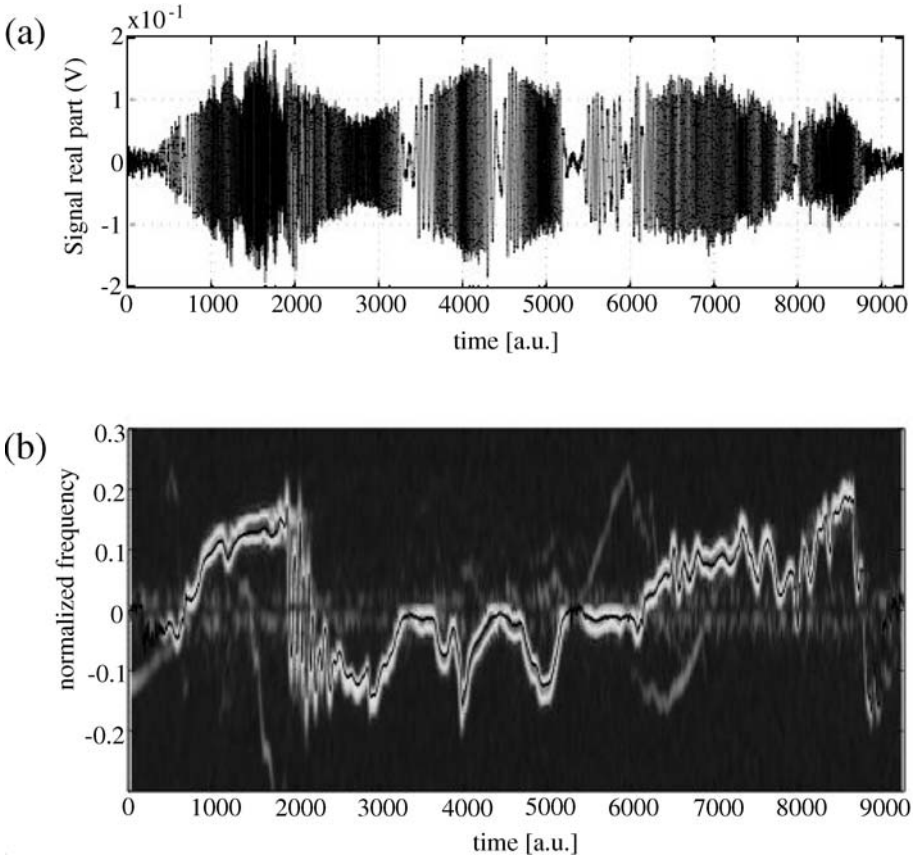

Fig. 20. Acoustic signal scattered by the moving particle. (**a**) Real part of the signal detected on one element of the transducer arrays. The signal shown has been heterodyned at the emission frequency ν_0. (**b**) Time frequency picture (spectrogram) of the same signal. The *solid black line* is the output of the high resolution parametric algorithm

quency ν_0 , the scattered sound at the receiver has frequency $\nu(t) = \nu_0 + \vec{q}.\vec{v}(t)$, where $\vec{v}(t)$ is the velocity of the tracer particle and $\vec{q}$ is the scattering wave vector.

A von Kármán swirling flow, similar to the used for the study of vorticity filaments (cf. Sect. III.C) is used to generate a strong turbulence in a confined volume (Fig. 19a). It is seeded with a single neutrally buoyant tracer particle (density of 1.06) with a diameter equal to 250 μm. The particles act as Lagrangian tracers for times longer than 1 ms (below which inertia cuts off their response), up to times as long as the particles stay confined inside the measurement volume (in practice this turns out to be several rotation periods of the driving disks). The flow is insonified at 2.5 MHz, with a single transducer element located at the flow wall in the mid-plane. The two receiver arrays are made of nine elements forming a cross and they are located at 45 degrees on each side of the emission direction. The measurement region is the intersection of the emission and detection cones. By direct triangulation (measurement of the phase shift of the sound detected between each element of the transducer arrays) one tracks the position of the tracer particle. Trajectories as shown in Fig. 19(b,c) are obtained. Very intense particle accelerations (over $4000\,\mathrm{m/s^2} \equiv 400\,\mathrm{g}$!) are measured when the particles wind around a vortex such as in Fig. 19c.

The detection of the particle velocity is much less straightforward. Simply computing the time derivative of the position would induce too much noise for an accurate study of Lagrangian velocity fluctuations in turbulence. Instead, one uses the Doppler shift of the scattered signal, which appears as a frequency modulation on the scattered sound detected centered on ν_0. This is observed in Fig. 20a: the rapid oscillations correspond to a large Doppler shift and hence a large particle velocity, whereas the quiet period corresponds to small particle velocities. In order to extract the frequency modulation, standard time-frequency analysis proves to be rather ill-adapted because of the nonstationarity and low oversampling of the signal. Instead one uses a high-resolution parametric algorithm [53], which rests

on the assumption that the scattered signal is a sine modulation embedded in noise (see Fig. 20b for results).

Altogether, this technique has been used to obtain the first measurements of Lagrangian velocity statistics in fully developed turbulence at high Reynolds numbers [54]. They have shown that intermittency is very intense in the Lagrangian domain and that it traces back to the development of long-time correlations in the Lagrangian dynamics [55].

V Concluding remarks

The study of sound-flow interactions has bought about new methods of flow inspection that have been used for simple and complex/turbulent flows, and applied both in the laboratory and in natural environments. When compared to optical techniques, sound measurements have the advantage of being made by transducers that are phase-sensitive (in addition to being able to work in opaque fluids). As a result, interferometry measurements are easily implemented, with the possibility of tuning the sound wavelength to probe selected scales of the flow under investigation.

As in the case of electromagnetic waves, theoretical descriptions give a clear understanding of the behavior in selected limits of the ratio of the wavelength to a characteristic size of inhomogeneities in the medium. Some cases have been reviewed here theoretically and experimentally, in simple, canonical, situations. When the sound wavelength is small compared to a length scale characteristic of the velocity gradients, one can use the formalism developed for ray propagation. The wavefronts are locally advected by the fluid velocity, and the phase unwrapped along ray paths. One finds that the dominant contribution comes from the antisymmetric part of the velocity gradient tensor, i.e., the flow vorticity. The canonical example is thus the propagation of monocromatic sound waves across an isolated vortex, as considered in Sect. II. There is a very good agreement between the analytical expressions derived for amplitude and phase evolution of the wavefronts, the measurements and numerical simulations of the problem. Vortex core size and strength can be derived from the measurement (Sect. II.B), as well as the actual vorticity profile under the assumption of axisymmetry [20, 21]. It would be interesting to compute and measure the secondary contributions to sound transmission coming form the symmetric part of the velocity gradient tensor. Experimentally, this may prove to be very difficult because flows that are forced to be vorticity free prove to be highly unstable and tend to naturally form vortices [56].

As the wavelength increases, the problem of sound transmission across a vortex whose core size if of the order of the wavelength is then made increasingly more complicated. The effects associated with scattering must be taken into account in addition to the effects of advection. Several numerical studies of this problem have been made [22, 23, 57, 58], and the matter certainly deserves further investigation. The scattering effect can be isolated if one changes the flow geometry to generate a crystal of vortices, each with a core size much smaller than the sound wavelength, as we have done in Sect. III.A. In this case, the measurements firmly establish the scattering theory developed by Lund and coworkers [9, 26] in the spirit of the original Lighthill work on sound generation. The scattering technique has been thoroughly used for the study of turbulence in the atmospheric boundary layers [43–45] and is now routinely applied in the study and monitoring of the environment [61]. The implementation of spectroscopy measurements in which several modes are simultaneously resolved in time has recently enabled new avenues in the study of the non linear dynamics of coherent structures, as shown in Sect. III.C. However, it should be noted that the results and experiments above assume a diluted distribution of vorticity, so that a single scattering approximation holds. The case of scattering by dense populations of vortices has been treated analytically [59, 60, 62], and deserves further experimental investigations.

One of the main difficulties of the acoustic measurements is that the scattering cross section by vortices (the dominant effect in an isothermal flow) is very small (often less than 10^{-5} of the incident sound pressure amplitude). As a result, several techniques have been developed in which the flow is seeded with small echogenic particle, i.e., particles whose an acoustic impedance significantly differs from that of the fluid, such as air bubbles in liquid flows or glass beads in gas flows. This method, besides being routinely used in commercial Doppler acoustic anemometers (DOP), has been recently applied to generate new velocity measurements. The acoustic speckle interferometry (described in Sect. IV.B) yields time resolved measurements that cannot be accessed by DOP anemometers. The acoustic tracking of tracers (Sect. IV.C) is a first step to-

wards the experimental study of fluid motion in Lagrangian coordinates. The initial work has been done in homogeneous turbulent flows, but the case of the entrainment of dense or light particles in inhomogeneous, anisotropic flows may be more relevant for practical applications.

Acknowledgments. The measurements reported are collected from work done since 1990 and published by several collaborators: C. Baudet (LEGI, Grenoble), F. Chillà (ENS, Lyon), S. Ciliberto (ENS, Lyon), B. Dernoncourt (Saint-Etienne), S. Fauve (ENS, Paris), R. Labbé (Univ. Chile, Santiago), P. Metz (ENS, Lyon), O. Michel (Univ. Nice), N. Mordant (ENS, Paris). The results reported in Sect. IV.A come from work done by C. Baudet, O. Michel and W.J. Williams. The results reported in Sect. IV.B come from work done by S. Manneville, L. Sandrin and M. Fink. We are most grateful to all authors for making their results available for this review.

References

1. Morse, P.M., Ingard, K.U.: *Theoretical acoustics*. Princeton University Press, NJ (1968)
2. Pinton, J.-F.: *Sound-Flow Interactions*. In: Auregan, Y., Maurel, A., Pagneux, V., (eds.) Springer Lecture Notes in Physics **586**. Springer Berlin Heidelberg New York (2002)
3. Blockintzev, D.: J. Acoust. Soc. Am. **18**, 322 (1945)
4. Lindsay, R.B.: J. Acoust. Soc. Am. **20**, 89 (1948)
5. Landau, L.D., Lifschitz E.M.: Fluid Mechanics, Pergamon Oxford, UK (1959)
6. Lighthill, M.J.: Proc. R. Soc. London **211**, 564 (1952)
7. Howe, M.: In *Sound-Flow interactions*. Lecture Notes in Physics LNP585. Springer Berlin Heidelberg New York (2002)
8. Möring, W.: J. Fluid Mech. **85**, 685 (1978)
9. Lund, F., Rojas C.: Physica D **37**, 508 (1989)
10. Bergmann, P.G.: J. Acoust. Soc. Am. **17**, 329 (1946)
11. Candel, S.M.: J. Fluid Mech. **90**, 465 (1979)
12. Karweit, M., Blanc-Benon, P., Juvé, D., Comte-Bellot, G.: J. Acoust. Soc. Am. **89**, 52 (1991)
13. Zandbergen, P.J., Dijkstra, D.: Ann. Rev. Fluid Mech. **19**, 465 (1987)
14. Labbé, R., Pinton, J.-F., Fauve, S.: Phys. Fluids **8**, 914 (1996)
15. Wunenberger, R., Andreotti, B., Petitjeans, P.: Exp. Fluids **27**, 181 (1999)
16. Anke, D.: Acustica **30**, 30 (1974)
17. Berry, M., Chambers, R.G., Large, M.D., Upstill, C., Walmsley, J.C.: Eur. J. Phys. **1**, 154 (1980)
18. Labbé, R., Pinton, J.-F.: Phys. Rev. Lett. **81**, 1413 (1999)
19. Brillant, G., Chillà, F., Pinton, J.-F.: Eur. Phys. J. B. **37**, 229–239 (2003)
20. Manneville, S., Robres, J.H., Maurel, A., Petitjeans, P., Fink, M.: Phys. Fluids **11**, 3380 (1999)
21. Manneville, S., Maurel, A., Roux, P., Fink, M.: Eur. Phys. J. B. **9**, 545 (1999)
22. Colonius, T., Lele, S.K., Moin, P.: J. Fluid Mech. **260**, 271 (1994)
23. Berthet, R.: Dissertation, École Normale Supérieure de Lyon (2001)
24. Chu, B.T., Kovásznay, L.S.G.: J. Fluid Mech. **3**, 494 (1958)
25. Fabrikant, A.L.: Sov. Phys. Acoust. **29**, 152 (1983)
26. Lund, F.: Phys. Fluids **9**, 1521 (1989)
27. Contreras, H., Lund, F.: Phys. Lett. A **67**, 127 (1990)
28. Petrossian, A., Pinton, J.-F.: J. Phys. II France **7**, 801 (1997)
29. Ford, R., Llewellyn-Smith, S.G.: J. Fluid Mech. **386**, 305 (1999)
30. Schaeffer, J.W., Eskinazi, S.: J. Fluid Mech. **6**, 241 (1959)
31. Gromov, P.R., Ezerskii, A.B., Fabrikant, A.L.: Sov. Phys. Acoust. **28**, 552 (1982)
32. Baudet, C., Ciliberto, S., Pinton, J.-F.: Phys. Rev. Lett. **67**, 193 (1991)
33. Pinton, J.-F.: Dissertation. École Normale Supérieure de Lyon (1993)
34. Pinton, J.-F., Baudet, C., Ciliberto, S.: In: *Turbulence in Spatially Extended System*. Nato Editions, Les Houches (1993)
35. Siggia, E.D.: J. Fluid Mech. **107**, 375–406 (1981)
36. Verzicco, R., Jimenez, J.: J. Fluid Mech. **394**, 261 (1999)
37. Frisch, U.: *Turbulence*. Cambridge University Press, Cambridge, England (1995)
38. Chainais, P., Abry, P., Pinton, J.-F.: Phys. Fluids **11**, 3524–3539 (1999)
39. Dernoncourt, B., Pinton, J.-F., Fauve, S.: Physica D **117**, 181–190 (1998)
40. Douady, S., Couder, Y., Brachet, M.-E.: Phys. Rev. Lett. **67**, 983–986 (1991)
41. Fauve, S., Laroche, C., Castaing, B.: J. Phys. II France **3**, 271–278, (1993)
42. Cadot, O., Douady, S., Couder, Y.: Phys. Fluids A **7**, 630–646 (1995)
43. Kallistratova, M.A., Keder, J., Petenko, I.V., Tieme, N.: Izv. Atmos. Oceanic Phys. **21**, 380–383 (1985)
44. Kallistratova, M.A., Petenko, I.V., Shurygin, Y.A.: Izv. Atmos. Oceanic Phys. **23**, 339–346 (1987)
45. Kallistratova, M.A.: Int. J. Remot. Sens. **15**, 251–266 (1994)
46. Ferziger, J.H.: J. Acoust. Soc. Am. **56**, 1705 (1974)
47. Brun, C., Pumir, A.: Phys. Rev E **63**, 056313 (2001)

48. Baudet, C., Michel, O.: In: *Advances in Turbulence VI*. Gavrilakis, S. (ed.), Kluwer Dordrecht (1996), p. 241
49. Baudet, C., Michel, O., Williams, W.J.: Physica D **128**, 1 (1999)
50. Williams, W.J., Jeong, J.: In: *Time-frequency signal analysis*. Longman, NY (1992)
51. Sandrin, L., Manneville, S., Fink, M.: Appl. Phys. Lett. **78**, 1155 (2001)
52. Manneville, S., Sandrin, L., Fink, M.: Phys. Fluids **13**, 1683 (2001)
53. Mordant, N., Michel, O., Pinton, J.-F.: J. Acoust. Soc. Am. **112**, 108–119 (2002)
54. Mordant, N., Michel, O., Metz, P., Pinton, J.-F.: Phys. Rev. Lett. **87**(21), 214 501 (2001)
55. Mordant, N., Delour, J., Arnéodo, A., Michel, O., Pinton, J.-F.: Phys. Rev. Lett. **89**(25), 254 502 (2002)
56. Andreotti, B., Douady, S., Couder, Y.: J. Fluid Mech. **444**, 151 (2001)
57. Berthet, R., Astruc, D.: J. Comp. Phys. **64**, 64 (2003)
58. Berthet, R., Fauve, S., Labbé, R.: Eur. Phys. J. B **32**, 237 (2003)
59. Baffico, M., Boyer, D., Lund, F.: Phys. Rev. Lett. **80**, 2590 (1998)
60. Boyer, D., Baffico, M., Lund, F.: Phys. Fluids **11**, 3819 (1999)
61. Kallistratova, M.A., Couletr, R.: Meteorol. Atmos. Phys. **85**, 21 (2004)
62. Snieder, R.: Coda wave interferometry. In: *2004 McGraw-Hill Yearbook of Science and Technology* 54, McGraw-Hill New York (2004)